IEEE Open Journal of
Antennas and Propagation   IEEE OPEN JOURNAL OF ANTENNAS AND PROPAGATION, VOL. 5, NO. 4, AUGUST 2024

942

Experimental Phase-Encoded Linear Sampling Method Imaging With a Single Transmitter and Receiver

MATTHEW J. BURFEINDT (Senior Member, IEEE), HATIM F. ALQADAH, AND SCOTT ZIEGLER[ID]

Radar Division, U.S. Naval Research Laboratory, Washington, DC 20375, USA

CORRESPONDING AUTHOR: M. J. BURFEINDT (e-mail: matthew.j.burfeindt.civ@us.navy.mil)

ABSTRACT The phase-encoded linear sampling method (PE-LSM) is an inverse scattering technique for reconstructing the shape of a conducting target from scattered electric fields. It is a variant of the well-known linear sampling method (LSM), which solves the nonlinear shape reconstruction problem using linear optimization. The PE-LSM mitigates the primary obstacle to practical imaging via LSM-based processing – its need for copious multistatic-multiview transmit-receive channels. In this study, we evaluate the PE-LSM using experimental data. We collect synthetic aperture data in an anechoic chamber using only a single transmit-receive channel. With the aid of a monostatic-to-multistatic transform, we generate reconstructions of each target via the PE-LSM. The results evince significant improvements in fidelity to the true target geometries compared to imagery generated by both conventional LSM processing and a conventional backprojection-based radar approach.

INDEX TERMS Imaging, inverse scattering, beamforming.

I. INTRODUCTION

RECONSTRUCTING the shape of highly conducting targets from scattered fields is of interest for a variety of applications related to the sensing and interrogation of man-made objects, including non-destructive evaluation and target identification. In principle, target reconstruction may be performed by estimating the spatial distribution of electrical properties in the scene via a quantitative inverse scattering technique [1], [2], [3], [4], [5]. However, for perfectly electrically conducting (PEC) or near-PEC targets, it can be advantageous to reconstruct only their shape, as their distribution of electrical properties is generally non-informative. In addition, quantitative techniques may fail to converge or require many iterations due to the inherent high contrast of PEC targets.

Techniques for reconstructing the shapes of conducting targets have been proposed in previous studies. Multiple nonlinear optimization approaches have been developed, including techniques based on local shape functions [6], [7], [8], subspace optimization [9], [10], [11], [12], and level sets [13], [14], [15]. Other approaches have used sparse optimization to estimate the locations of equivalent

current distributions on the target surface [16], [17], [18], [19], [20], [21]. Physical-optics-based approaches have used high-frequency approximations to simplify the inverse problem [22], [23], [24].

The linear sampling method (LSM) in particular has received significant attention for target shape reconstruction [25], [26], [27], [28], [29], [30], [31], [32], [33], [34], [35]. The LSM involves solving for a set of transmit weights for every pixel in the domain in order to induce specified elementary radiation patterns from the target. The change in the solution norm between pixels that are inside or outside the target support allows for discerning the target shape. Solving for the weights allows the LSM in its conventional formulation to avoid the Born approximation. In addition, solving for the weights is a linear problem, and thus the LSM is relatively straightforward to implement.

However, practical LSM imaging is hampered by its sensor geometry requirements. Robust LSM imaging typically requires multistatic-multiview sensor configurations with dense spatial sampling and wide angular coverage of the target. LSM performance tends to degrade for data acquisition scenarios that use only a few physical

sensors. The spatial sensor diversity required by the LSM is challenging to realize in some scenarios due to cost or complexity.

In principle, sensor configurations based on synthetic apertures present a beneficial compromise between hardware resources and data diversity. In such configurations, one or only a few sensors travel through an aperture while collecting scattered field data at regular intervals. Significant angular diversity in the received data may be achieved if the aperture has a substantial angular span. However, even with significant synthetic aperture lengths, the fidelity of the LSM image is expected to degrade relative to scenarios that include a full complement of multistatic-multiview sensors.

Degradation may be most severe in limited-aperture scenarios, in which the synthetic aperture is limited to viewing one side of the target. In such geometries, much of the signal range information (i.e., signal information related to the direction of propagation orthogonal to the array) is contained in the change in phase across frequencies. The conventional LSM has no mechanism for leveraging this information coherently, unlike conventional radar processing approaches such as backprojection. The LSM solution is instead typically formed at each frequency individually and then the solution frequency components are summed non-coherently. This can lead to a loss of range information in the LSM imagery, resulting in target responses that are significantly extended in the range direction [36], [37], [38]. These effects may limit the utility of the LSM for applications where it is not possible to view the target from all sides due to physical constraints on sensor placement or constraints on data acquisition time.

We have previously presented a new variant of the LSM that mitigates the challenges posed by synthetic apertures and limited apertures. The phase-encoded LSM (PE-LSM) [38] includes two enhancements that are partially inspired by conventional radar processing concepts. The first is an initial receive beamforming step (or, equivalently, a receive matched filtering step across aperture samples) that stabilizes the solution for limited-sensor scenarios. The second is a constraint that enforces a coherent propagation-based relationship for the phase of the solution across frequency. This constraint incorporates improved range information into the LSM optimization, which is especially critical for limited-aspect scenarios. The beamforming enhancement and the phase-delay constraint account for free-space propagation to the target surfaces, but not the change in wavelength and thus electrical path-length caused by propagation inside of a dielectric target, and thus the PE-LSM is most promising for imaging the surfaces of conducting targets.

Our previously work on the PE-LSM [38], [39], [40] demonstrated significant improvements in image fidelity from synthetic-aperture and limited-aperture data acquisitions compared to conventional LSM processing. However, these previous studies used mostly simulated data, except for a single experimental example in [38] that used a geometrically simple target in the form of a conducting sphere. Other previous experimental work on LSM imaging from synthetic apertures has also used targets with modest geometrical complexity in the range direction [41], [42].

In this paper, we present a more advanced experimental study. We collect experimental data in an anechoic chamber using an inverse synthetic aperture strategy, in which the sensors are stationary and the target rotates during data acquisition in order to generate signal angular diversity. We use multiple conducting targets with a variety of scattering features and thus greater geometrical complexity compared to our previous experimental results.

We make an additional experimental advancement by limiting our sensor configuration to a single transmitter and a single receiver oriented to collect data in the monostatic direction. Previous PE-LSM synthetic aperture results included multiple receivers separated by several degrees in the aperture. We avoid the need for multiple receivers by enhancing the PE-LSM via a pre-processing step that synthesizes virtual multistatic data from collected monostatic data. This monostatic-to-multistatic transform, which is a simplified version of the transform we previously described in [43], [44], relies on the high degree of information redundancy available from closely spaced receivers moving through a synthetic aperture. Forming images from purely monostatic data is of interest for reducing hardware complexity and cost as much as possible. It also allows for avoiding complications related to calibrating multiple receive channels.

We image the experimental data and evaluate the PE-LSM performance relative to standard LSM processing and backprojection processing. The comparison to both conventional techniques is of interest as the PE-LSM leverages concepts underpinning both the LSM as well as radar signal processing due to its two radar-inspired enhancements. We have previously demonstrated improvements in image fidelity for the PE-LSM compared to backprojection [39], [40]. However, these previous studies used exclusively simulated data.

We use our own experimental data for this study instead of leveraging public datasets that have previously been widely explored [45], [46]. These public datasets are of limited utility for our study for several reasons. They use only a few conducting targets, almost all of which are of minor geometrical complexity. The setup from [46] also includes no receivers in the backscatter direction. Data from monostatic azimuth angles are relevant for exploring limited synthetic aperture geometries which are of interest for this study.

In addition, the data in [45], [46] are limited to targets of modest electrical dimension, whereas in our experiments we choose frequencies at which the targets are electrically large (i.e., up to 40 wavelengths). Such targets are especially challenging for LSM-based processing, as increases in electrical size typically exacerbate the requirement of the conventional LSM for copious multistatic spatial samples. However, using wavelengths that are small compared to the target dimension is of interest for achieving finer detail on the target structure.
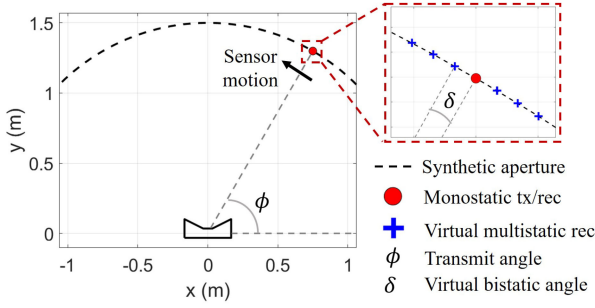
FIGURE 1. A diagram of the equivalent imaging geometry.

The remainder of this paper is laid out as follows. We present our algorithmic methods in Section II. We then describe our experimental data acquisitions in Section III. We then present our imaging results in Section IV. Lastly, we make concluding statements in Section V.

II. ALGORITHMIC FORMULATION

A. IMAGING GEOMETRY

We generate angular diversity in this study by rotating the target while keeping the sensors stationary for ease of experimentation. However, it is convenient to present our imaging formulation and analyze imaging results in the equivalent frame in which the target is stationary and the sensors move around it in a synthetic aperture.

This equivalent imaging geometry is illustrated in Fig. 1. A single monostatic sensor travels across the synthetic aperture. The synthetic aperture as illustrated has an angular span of 90°, but we also use apertures of near-complete spans of 350° in this study. At regular pulse repetition intervals the sensor radiates an incident field and then collects the resulting scattered field from the target. At any given point in the aperture, the angular position of the sensor is denoted via angle ϕ, which is measured counterclockwise from the +x-axis.

Also pictured in Fig. 1 are a collection of virtual receivers. These are fictitious receivers whose data is synthesized from the monostatic collected data via the monostatic-to-multistatic transform that we discuss in Section II-D. The positions of the virtual receivers travel through the aperture along with the true monostatic sensor while maintaining constant angular spacing. The bistatic angular offset from the monostatic sensor for a given virtual receiver is denoted by δ.

B. LSM FUNDAMENTALS

The goal of the conventional LSM is to solve for a transmit beamforming vector for every individual pixel in the scene. The desired effect of the weighting of the transmitted signal is to induce the target to re-radiate the same field as an elementary current source at the focus pixel location. The rationale for this approach is that it can be shown via mathematical [25] or electromagnetic [34], [35] arguments that (assuming sufficient transmit-receive spatial samples) a

low-norm solution to the beamforming weight can only be found if the elementary pattern to synthesize is located within the target support. Thus, an image of the target support may be formed by rastering the focus location through every pixel in the scene, solving the beamforming problem, and then plotting an indicator function of the solution norm at each pixel. In this subsection, we outline our implementation of conventional LSM.

1) THE LSM SYSTEM OF EQUATIONS

We assume a set of N_{tx} transmit positions and N_{rec} receive positions surrounding the unknown target. The scattered field for the various multistatic transmit-receive position pairs is collected at wavenumber k and placed in the $N_{\text{rec}} \times N_{\text{tx}}$ matrix $\mathbf{E}(k)$. For ease of explication, in this study we assume 2D transverse magnetic (TM) propagation, and thus each collected scattered field phasor is assumed to be a scalar.

In most LSM studies, the sensors are stationary and each transmit and receive position corresponds to a single physical sensor. Thus, assuming the scattered field phasors are collected for every transmit-receive pair, then every element in $\mathbf{E}(k)$ is filled. For a synthetic-aperture configuration in which only one or a few sensors travel through a number of transmit-receive locations, only a subset of the $N_{\text{rec}} \times N_{\text{tx}}$ possible multistatic phasors are collected. We account for this configuration using a strategy that has been used in multiple previous studies, wherein the collected phasors are entered into $\mathbf{E}(k)$ and the elements corresponding to uncollected pairs are left as zeros [36], [38], [41], [42].

For purely monostatic data, the result would be a matrix with entries only on its main diagonal. For a multistatic synthetic aperture wherein the receivers travel with the transmitter while maintaining constant angular spacing, the matrix is in the form of a multi-diagonal matrix. Further explication and illustration of our implementation of this strategy can be found in [38, Sec. II-B and Fig. 2].

The LSM transmit beamforming problem involves finding a solution to the following system of linear equations,

$$\mathbf{E}(k)\mathbf{g}(k, \mathbf{r}) = \mathbf{\Phi}(k, \mathbf{r}), \qquad (1)$$

where $\mathbf{r}$ is a pixel location in the domain, $\mathbf{\Phi}(k, \mathbf{r})$ is the $N_{\text{rec}} \times 1$ vector of Green's functions between $\mathbf{r}$ and each receive location, and $\mathbf{g}(k, \mathbf{r})$ is the unknown $N_{\text{tx}} \times 1$ vector of transmit beamformer weights we wish to find. A distinct linear system is solved for each $\mathbf{r}$ and each k of interest.

In this study, we use a normalized Green's function given by

$$\mathbf{\Phi}(k, \mathbf{r}) = \mathbf{\Phi}_0(k, \mathbf{r})/||\mathbf{\Phi}_0(k, \mathbf{r})||. \qquad (2)$$

Here, as in the remainder of this paper, the norm is taken across the elements of the vector, and thus in this case across the receivers. The normalization in (2) has been used in previous studies in order to improve LSM imaging performance in limited-aperture scenarios [38], [47]. We employ it here as several of our experimental examples use

limited synthetic apertures. The mth element of $\mathbf{\Phi}_0(k, \mathbf{r})$ is the Green's function for the mth receiver, given by

$$\Phi_0^m(k, \mathbf{r}) = H_0^2\big(kd_{\text{rec}}^m(\mathbf{r})\big), \tag{3}$$

where $H_0(\cdot)$ is the zeroth-order Hankel function of the second kind and $\mathbf{d}_{\text{rec}}(\mathbf{r})$ is the $N_{\text{rec}} \times 1$ vector of distances from $\mathbf{r}$ to each receive location.

The solution to (1) is typically found via a regularized approach, such as the well-known Tikhonov method, given by

$$\min_{\mathbf{g}(k,\mathbf{r})} ||\boldsymbol{\rho}(k, \mathbf{r})||^2 + \alpha ||\mathbf{g}(k, \mathbf{r})||^2, \tag{4}$$

where $\boldsymbol{\rho}(k, \mathbf{r}) = \mathbf{E}(k)\mathbf{g}(k, \mathbf{r}) - \mathbf{\Phi}(k, \mathbf{r})$ is the residual vector to (1) and α is a regularization parameter that controls the degree to which large-norm solutions are penalized.

2) THE INDICATOR FUNCTION

After (4) is computed for every k and $\mathbf{r}$ of interest, an image of the target support can be generated using an indicator function of the LSM solution norm. Multiple indicator functions have been proposed in past work. The indicators frequently follow a form similar to

$$I(\mathbf{r}) = \sum_i ||\mathbf{g}(k_i, \mathbf{r})||^{-p}, \tag{5}$$

where $p = 1$ or 2 [31]. In previous limited-aperture studies [38], [39], we have used a modified indicator function given by

$$I(\mathbf{r}) = \left(\sum_i \frac{||\mathbf{g}(k_i, \mathbf{r})||^2}{\max_{\mathbf{r}'} ||\mathbf{g}(k_i, \mathbf{r}')||^2} \right)^{-1}, \tag{6}$$

where k_i is the ith collected wavenumber and the norms are over the transmitters. This indicator is nearly identical to the indicator used in other limited-aperture LSM studies [41], [47], with the exception that the reciprocal is taken in order to conform with the common convention that the indicator function is large inside the target support and small outside of it. The normalization of the indicator according to the maximum norm across $\mathbf{r}'$ has been shown in some cases to improve limited-aspect performance by helping to differentiate the signals in range [47].

An interesting recent study [48] has proposed an alternative indicator that uses the product across frequency as opposed to the sum, given by

$$I(\mathbf{r}) = \prod_i ||\mathbf{g}(k_i, \mathbf{r})||^{-1}. \tag{7}$$

Using the product instead of the sum can increase the contrast between target features and artifacts in the background. However, there is a potential trade-off in that it may also exacerbate the contrast between features on the target that evince different scattering amplitudes. This effect may be more pronounced for electrically large targets that have multiple types of scattering features, as in this study. In addition, to our knowledge the product-based indicator has

not been studied closely for sensor configurations using synthetic aperture data acquisitions with few sensors.

In this study, we display results from only one indicator function for conciseness. We choose (6) to maintain consistency with previous limited-aperture work. We leave study of (7) for limited aspects, synthetic apertures, and electrically large targets for future work.

C. PE-LSM

The PE-LSM solution is found by solving the problem given by

$$\min_{\mathbf{g}(k,\mathbf{r})} \quad \sum_i \left| \mathbf{w}_{\text{rec}}^{\text{H}}(k_i, \mathbf{r})\boldsymbol{\rho}(k_i, \mathbf{r}) \right|^2 + \alpha ||\mathbf{g}(k_i, \mathbf{r})||^2$$
$$+ \beta ||\boldsymbol{\gamma}(k_i, \mathbf{r})||^2, \tag{8}$$

where the sum is over all collected k, $\mathbf{w}_{\text{rec}}(k, \mathbf{r})$ is a receive-beamforming vector applied to the residual, $\boldsymbol{\gamma}(k, \mathbf{r})$ is a constraint vector, and β is a second regularization parameter. This minimization is thus equivalent to (4) with the two enhancements of the beamforming step and the additional constraint. The two enhancements, when used in concert, allow for improved-fidelity LSM-style imaging from synthetic apertures. We describe each enhancement below.

The receive beamforming vector in (8) is given by

$$\mathbf{w}_{\text{rec}}(k, \mathbf{r}) = \exp(-jk\mathbf{d}_{\text{rec}}(\mathbf{r})), \tag{9}$$

where $\mathbf{d}_{\text{rec}}(\mathbf{r})$ is defined as in (3). Applying this beamforming vector to the data focuses the receive array on $\mathbf{r}$ prior to solving the optimization in (8). We hypothesize that this focusing operation decreases the allowable complexity of the solution space by emphasizing signal contributions from the vicinity of $\mathbf{r}$ and de-emphasizing signal contributions from features at different spatial locations. This improves the robustness of the optimization when there are also limited degrees of freedom in the measured data due to limited receive data for each transmit location.

The additional constraint vector in (8) is given by

$$\boldsymbol{\gamma}(k, \mathbf{r}) = \mathbf{g}(k, \mathbf{r}) - \mathbf{g}(k + \Delta k, \mathbf{r}) \odot \exp(-j\Delta k\mathbf{d}_{\text{tx}}(\mathbf{r})), \tag{10}$$

where Δk is the step size between adjacent wavenumbers, '$\odot$' refers to point-wise multiplication, and $\mathbf{d}_{\text{tx}}(\mathbf{r})$ is the vector of distances between $\mathbf{r}$ and each transmit location. As $\mathbf{g}(k, \mathbf{r})$ is essentially a transmit beamforming weight applied to the data, this constraint encourages solutions that take into account the expected change in phase across frequency due to propagation of the incident wave in the background. Linking the solution at adjacent frequencies in this manner effectively provides *a priori* information to the optimization that stabilizes the solution for scenarios with limited receive samples. In addition, it takes into account the coherent change in the signal across frequency, which allows for leveraging the signal range information more effectively than conventional LSM processing.

We solve (8) in a straightforward manner via the block-matrix formulation given by

$$\min_{\mathbf{x}} ||\mathbf{A}\mathbf{x} - \mathbf{b}||^2. \quad (11)$$

The block matrices in (11) are given by

$$\mathbf{b} = \begin{bmatrix} \mathbf{w}^{\mathrm{H}}(k_1, \mathbf{r})\Phi_0(k_1, \mathbf{r}) \\ \vdots \\ \mathbf{w}^{\mathrm{H}}(k_F, \mathbf{r})\Phi_0(k_F, \mathbf{r}) \\ \mathbf{0} \end{bmatrix} \mathbf{x} = \begin{bmatrix} \mathbf{g}(k_1, \mathbf{r}) \\ \vdots \\ \mathbf{g}(k_F, \mathbf{r}) \end{bmatrix}$$

$$\mathbf{A} = \begin{bmatrix} \mathbf{A}_0 \\ \sqrt{\alpha}\mathbf{I} \\ \sqrt{\beta}\mathbf{D} \end{bmatrix}, \quad (12)$$

where $k_1, \ldots, k_F$ are the F wavenumbers used in the reconstruction, $\mathbf{I}$ is the $N_{\mathrm{tx}}F \times N_{\mathrm{tx}}F$ identity matrix, $\mathbf{0}$ is a vector of zeros of size $N_{\mathrm{tx}}(2F - 1) \times 1$, the block-matrix $\mathbf{A}_0$ is given by

$$\mathbf{A}_0 = \begin{bmatrix} \mathbf{w}^{\mathrm{H}}(k_1, \mathbf{r})\mathbf{E}(k_1) & & 0 \\ & \ddots & \\ 0 & & \mathbf{w}^{\mathrm{H}}(k_F, \mathbf{r})\mathbf{E}(k_F) \end{bmatrix}, \quad (13)$$

and $\mathbf{D}$ is a matrix of size $N_{\mathrm{tx}}(F - 1) \times N_{\mathrm{tx}}F$ wherein the main diagonal is filled with ones, the N_{tx}-diagonal is a concatenation of $F - 1$ copies of $\exp(-\Delta k\mathbf{d}_{\mathrm{tx}}(\mathbf{r}))$, and the remaining entries are zeros.

D. MONOSTATIC-TO-MULTISTATIC TRANSFORM

Achieving the best image fidelity with the PE-LSM requires a few receive samples to be collected for each transmit sample. In previous work [38], we have assumed a few physical receivers that translate through the synthetic aperture in concert with a single transmitter. However, achieving good results with only a single physical transmitter and receiver is of interest for reducing the hardware complexity of the imaging setup as much as possible.

As shown in [38], good image fidelity can be achieved if the receive samples are in the vicinity of the transmitter. This allows us to take advantage of the significant redundancy in signal information for closely spaced sensors by synthesizing virtual multistatic receive samples from the collected monostatic data. We perform this synthesis via the monostatic-to-multistatic transform that we describe below, which is a modest simplification of a transform that we have introduced in previous studies [43], [44].

The transform can be summarized intuitively in the following manner. For a given desired bistatic transmit receive pair, we find the monostatic data sample for which the wave undergoes the same expected phase delay while traveling from the transmitter, through the scene, and then back to the receiver. We then simply replace the desired bistatic sample in $\mathbf{E}(k)$ with this monostatic sample. Further mathematical development for this procedure is given as follows.

Under the Born and plane-wave approximations, the scattered field resulting from transmitting from an azimuth angle ϕ and observing from $\phi + \delta$, as in Fig. 1, can be written [49]

$$E(\delta, \phi, k) \approx \xi \int \int \sigma(x, y) \exp(-jk_x x - jk_y y) dx dy, \quad (14)$$

where $\sigma(x, y)$ is the contrast distribution in the imaging scene, ξ is a slowly varying and non-informative scalar, and the $x-$ and $y-$directed wavenumbers are given by

$$k_x = -k(\cos\phi + \cos(\phi + \delta))$$
$$= -2k\cos(\phi + \delta/2)\cos(\delta/2)$$
$$k_y = -k(\sin\phi + \sin(\phi + \delta))$$
$$= -2k\sin(\phi + \delta/2)\cos(\delta/2). \quad (15)$$

Clearly, the corresponding signal for a purely monostatic signal has the identical form as (14) with $\delta = 0$ in (15). Thus, the monostatic signal at wavenumber k_{m} and angle ϕ_{m} is approximately equivalent to the bistatic signal at k, ϕ, and δ if the following relationship holds:

$$2k_{\mathrm{m}}\cos\phi_{\mathrm{m}} = 2k\cos(\phi + \delta/2)\cos(\delta/2)$$
$$2k_{\mathrm{m}}\sin\phi_{\mathrm{m}} = 2k\sin(\phi + \delta/2)\cos(\delta/2). \quad (16)$$

It is straightforward to show that (16) is satisfied when

$$\tan\phi_{\mathrm{m}} = \tan(\phi + \delta/2)$$
$$k_{\mathrm{m}} = k\cos(\delta/2). \quad (17)$$

In our scenario of interest, δ can be assumed to be small, as the receivers are in the close vicinity of the transmitter for all transmit/receive positions in the synthetic aperture. Thus, we simplify (17) to

$$\phi_{\mathrm{m}} \approx \phi + \delta/2$$
$$k_{\mathrm{m}} \approx k. \quad (18)$$

Thus, assuming we have collected the monostatic data defined by $E(0, \phi, k)$, and desire to synthesize the bistatic data $E(\delta, \phi, k)$, we can simply extract the monostatic sample $E(0, \phi + \delta/2, k)$ and place it in the matrix element in $\mathbf{E}(k)$ corresponding to the angles δ and ϕ. If the monostatic data is not collected at the precise angle $\phi + \delta/2$, but is collected at adjacent angles, then the desired phasor can be extracted by a straightforward one-dimensional interpolation of $E(0, \phi, k)$ in ϕ. The interpolations are straightforward due to the synthetic-aperture setup of the imaging scenario, as the monostatic sensor passes through nearly all azimuth angles $\phi + \delta/2$ of interest while collecting data. The exceptions are receive points located outside of the synthetic aperture, which occur when the sensor is at the lowest angle of ϕ in the aperture and $\delta < 0$ or when the sensor is at the highest values of ϕ and $\delta > 0$. However, we address these edge samples by simply discarding them in (1).

In [43], [44], our previous formulation of the monostatic-to-multistatic transform allows for synthesizing virtual data from wider bistatic angles via a two-dimensional interpolation in both ϕ and k in some cases. However, handling of missing samples of the aperture is less straightforward.

As will be seen in the following sections, good imaging results are achieved via the PE-LSM using the simpler one-dimensional interpolation strategy given above. We thus leave the implications of the more complex two-dimensional scheme to PE-LSM processing to future work.

E. BACKPROJECTION

The sensing geometry for this study motivates the use of a backprojection implementation that mitigates the effects of anisotropic scattering, wherein the scattering behavior of target features changes with significant changes in sensor angle. Anisotropic scattering can pose challenges for backprojection-based imaging techniques, which often assume an isotropic point scatterer response at every pixel in the imaging scene. For instance, limited persistence of features across the aperture may result in degraded visual fidelity of the backprojection image due to varying cross-range resolution or dimming across the target footprint.

As described in Section II-A, this study includes image formation from near-complete circular apertures (i.e., with 350° of aspect) as well as apertures that form a shorter arc (i.e., with 90° of aspect). While the latter aperture size is more limited than is used for the vast majority of LSM studies, both aperture sizes illuminate significant portions of the target surface, and thus are of interest for reconstructing the target shape. The azimuth diversity of both choices of aperture has the potential to induce anisotropic scattering from the target.

We thus deploy a backprojection strategy for mitigating the effects of anisotropic scattering that is similar to a common approach from the radar imaging literature (e.g., [50], [51], [52]). We form backprojection images over a series of subapertures. We then assign the backprojection image value at each pixel according to the maximum response for that pixel across subapertures. As the degree of anisotropy is limited for each subaperture due to its relatively narrow angular span, image degradation from anisotropic effects is therefore decreased.

Our backprojection computation of the nth subaperture backprojection value for pixel location $\mathbf{r}$ is given by

$$I_n^B(\mathbf{r}) = \sum_i \sum_{l \in C_n} \sum_m E(\delta_m, \phi_l, k_i) h^*(\delta_m, \phi_l, k_i, \mathbf{r}), \quad (19)$$

where $E(\delta, \phi, k)$ has the same meaning as in (14), δ_m is the mth virtual receiver offset, ϕ_l is the lth transmit angle in the whole synthetic aperture, C_n is the set of transmit angle indices l composing the nth subaperture, and $h(\delta, \phi, k, \mathbf{r})$ is the backprojection filter acting on $E(\delta, \phi, k)$. The latter is defined by

$$h(\delta, \phi, k, \mathbf{r}) = \exp\left(-jk\left(d(\phi, \mathbf{r}) + d(\phi + \delta, \mathbf{r})\right)\right), \quad (20)$$

where $d(\phi, \mathbf{r})$ is the distance from $\mathbf{r}$ to the point in the synthetic aperture at angle ϕ. The final backprojection image is then given by

$$I^B(\mathbf{r}) = \max_n \left| I_n^B(\mathbf{r}) \right|^2. \quad (21)$$

F. PARAMETER SELECTION

Each imaging algorithm in this study requires the selection of one or more parameters. For the PE-LSM, the two parameters to select in (8) are α, which is a Tikhonov-like parameter that penalizes large-norm solutions, and β, which controls the influence of (10) on the optimization, i.e., the degree to which the desired propagation-based phase-delay relationship between frequencies is emphasized. In [38], we described a robust heuristic for selecting α and β that involves evaluating the behavior of the PE-LSM solution norm for a small subset of pixels across a range of regularization parameter values. We follow this strategy for this study. For conciseness, we refer the reader to [38] for a full treatment of the heuristic. Across the examples in this study, the heuristic results in $\log_{10} \alpha$ between -6 and -5 and $\log_{10} \beta$ between -2 and -1. This is consistent with our previous experience with the PE-LSM in that favorable results are achieved when β is greater than α by around three to five orders of magnitude.

The standard LSM also includes the Tikhonov parameter α. For each imaging example, we swept $\log_{10} \alpha$ from -13 to -6 and viewed the resulting indicator function. We found that selecting $\log_{10} \alpha = -10$ consistently resulted in regions of high indicator function in the general vicinity of target scattering features with at least some contrast with the background. Deviating from this value produced only modest differences in reconstruction quality, unless $\log_{10} \alpha$ was elevated to around -7 or above, in which case the images lose contrast with the background. The behavior of the solution thus obviates any benefits from choosing the regularization parameter via an automated method in this study. Thus, for simplicity, we simply select the indicators for $\log_{10} \alpha = -10$ for display in this paper.

The backprojection implementation given in Section II-E requires the selection of size and placement of the subapertures. We experimented with multiple subaperture sizes using the examples in this study ranging from 2.5° to 20°. We selected 5° subapertures for display, as this choice resulted in consistent focusing across each target surface and thus consistent visual fidelity to the true target shape. As in [50], we distributed the subapertures such that they overlapped their neighbors by 50%.

III. EXPERIMENTAL DATA ACQUISITION

A photograph of our experimental setup is given in Fig. 2(a). A target is placed on a rotational stage in an anechoic chamber. A single transmit antenna and a single receive antenna are mounted offset from the target by 1.5 m. Both antennas are standard gain horns. A detail photograph of the antennas is given in Fig. 2(b).

The antennas are connected to the two ports of a vector network analyzer (VNA). The VNA collects S_{21} signal phasors against the target as it rotates on the stage. For each target, we record phasors in rotational increments of 0.25° and across multiple frequencies starting at 35 GHz. The IF bandwidth of the VNA is set to 1 kHz during data

(a)

(b)

(c)

(d)

(e)

(f)
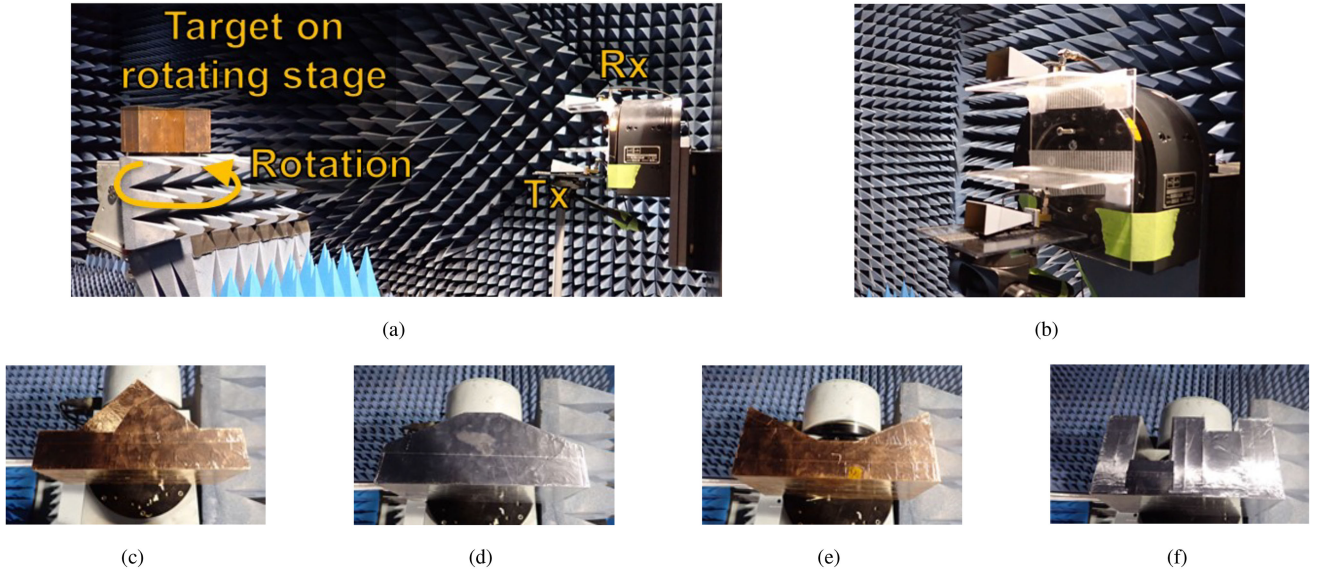
FIGURE 2. Photographs of (a) the experimental setup, (b) the antennas, (c) the platform-and-triangle target, (d) the convex target, (e) the concave target, and (f) the double-cavity target.

acquisition. Collection of all phasors across 350° of target rotation takes approximately $20-30$ minutes per target.

Figs. 2(c-f) are detail photographs of the targets used in this study. Each target is a 3D-printed cylinder that has been covered on all sides by either copper or aluminum conducting tape. The cross-sections of the cylinders are in the form of generic geometrical shapes with a variety of scattering features. The maximum dimension of each target cross-section is about 330 cm. Thus, the electrical sizes of the targets are around $35-40$ wavelengths at our chosen frequency of operation. This is significantly larger than the target size of most LSM studies, which typically use targets that are only a few wavelengths in size.

The platform-and-triangle target in Fig. 2(c) includes surfaces pointing in multiple azimuth directions as well as a prominent and sharp change in the direction of the scattering surface at the top of the triangle. The convex target in Fig. 2(d) also includes a raised but shallower shape pointed in the same direction. Imaging these somewhat similar but distinct shapes is useful in evaluating our ability to distinguish between different features in the imagery. Conversely, the concave target in Fig. 2(e), which is in the form of a shallow cavity, is of interest due to the well-known weakness of the conventional LSM in reconstructing non-convex shapes. Lastly, the double-cavity target in Fig. 2(f) allows us to evaluate the ability of the algorithms to reconstruct features at different ranges (i.e., the different depths of the cavities).

IV. RESULTS
A. IMAGES FROM 90-DEGREE ROTATIONS
We first consider the performance of each algorithm when the target undergoes a partial rotation. We select a 90° subset of the collected data. The resulting imaging scenario is equivalent to the limited synthetic-aperture scenario illustrated in Fig. 1, in which the sensors achieve only a partial view of the target.

We perform a few pre-processing steps prior to applying the imaging algorithm. We first subtract out a length of phase-delay in the data in order to remove the electrical path lengths of cables, connectors, or other components. We empirically choose the phase delay to compensate by adjusting it until the target responses are in the correct location in both the backprojection and PE-LSM images. We also apply a Doppler filtering operation to the data to remove stationary signal sources, such as residual direct-path signal from the transmitter to the receiver. We do not require any calibration of the incident field. Neither the PE-LSM nor the standard LSM require a high-fidelity model of the incident field in their formulation, as they are both so-called qualitative methods with no need for a forward solution.

We select 6 frequencies uniformly distributed across a bandwidth of 1.25 GHz. We use the monostatic-to-multistatic transform detailed in Section II-D to generate data from 7 virtual receivers at 0.75° angular spacing from the experimentally collected single-channel data. Unless otherwise stated, we use identical parameters for all subsequent subsections.

We then apply the resulting data to the standard LSM, backprojection, and PE-LSM algorithms. We form the imagery on a 60×60 cm domain on a grid of 35×35 pixels using (6) for the standard LSM and the PE-LSM and (21) for backprojection. We then upsample the images to a 70×70 grid of pixels for display. We lastly normalize each image to its most intense pixel and set the colorbars to range from zero to one.

The resulting images are shown in Fig. 3. In the local coordinate system used to plot the images, the aperture is centered on the $+y-$axis. Thus, the "tops" of the targets,
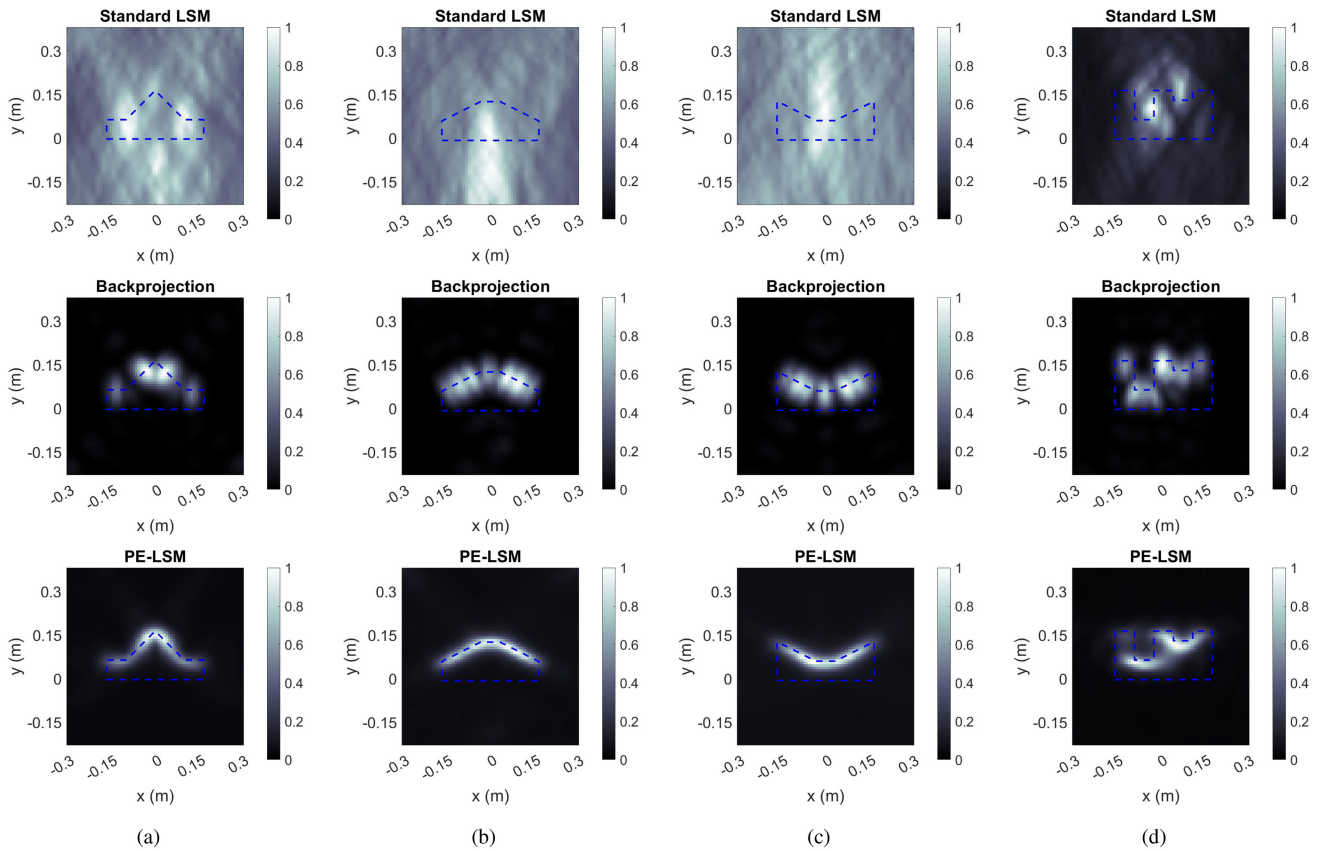
FIGURE 3. Images generated via the standard LSM, backprojection, and the PE-LSM using 90° apertures for the (a) pedestal-and-triangle, (b) convex, (c) concave, and (d) double-cavity targets. The aperture is centered on the $+y$-axis and the bandwidth is 1.25 GHz.

i.e., the target surfaces on the side of the target facing in the $+y-$direction, are illuminated.

The standard LSM images are of generally low fidelity across all four targets. There is some correlation between regions of high indicator function and the location of significant scattering features. However, there is not much detail on the target shape. For the convex and concave targets, the region of high indicator function is extended in the range direction (i.e., the $-y-$direction), which is consistent with previous limited-aperture LSM results in the literature [36], [37], [38]. The regions of high indicator function value also do not conform to the shape of the targets in the lateral dimension. For instance, in the image for the concave target, there is a high target response near the center of the target, but the indicator function along the two sides of its shallow cavity is indistinguishable from the background. There are also several prominent off-body artifacts in the images of the pedestal-and-triangle target and the double-cavity target.

The contrast with the background is relatively modest for the standard LSM images for all targets except for the double-cavity target, which may signify particularly high backscatter from the cavities. However, as seen by the image artifacts discussed above (poor range resolution, poor lateral conforming of the indicator with the target structure, and

the off-body responses), the poor fidelity of the standard LSM images is not merely a consequence of the modest contrast, but is perhaps more importantly a consequence of the low-fidelity distribution of apparent target structure in the imagery.

The backprojection images are of greater fidelity than the standard LSM images. The focused signal energy is concentrated along the illuminated surfaces of each target such that the overall shape of the surfaces can be broadly ascertained. The focused signal distribution appears as a series of discrete scattering centers localized near prominent scattering features as well as distributed along longer target contours. This latter effect is most likely due to the change of the specular reflection point along the longer surfaces that occurs as the subapertures advance through the synthetic aperture. The appearance of a series of concentrated scattering centers along long target contours is consistent with results from previous subaperture-based wide-angle radar imaging work [52]. The observed resolution in the range (i.e., down) direction is consistent with the nominal radar range resolution for a 1.25 GHz bandwidth, given by 12 cm.

The PE-LSM images are also of good fidelity, as high values of the indicator function are tightly concentrated along the illuminated surfaces of the target. However, there are
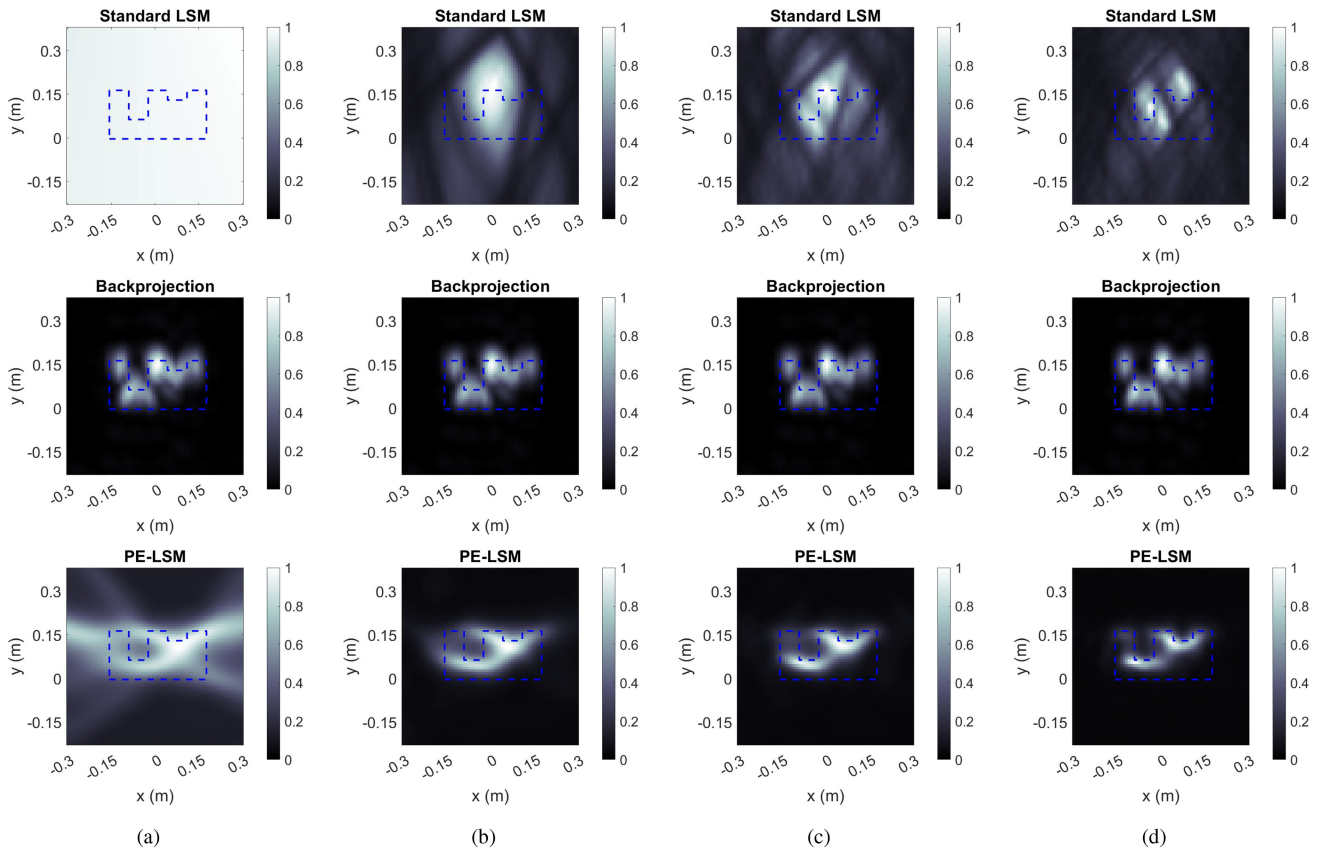
FIGURE 4. Images of the double-cavity target from 90° apertures for (a) 0, (b) 2, (c) 4, and (d) 8 virtual receivers.

two important differences between the backprojection and PE-LSM images. The first difference is that the apparent resolution in the range or down direction is significantly finer compared to the backprojection images. This is consistent with our previous results from simulated data [39], [40].

The finer resolution may be due to the similarity in form between LSM-style processing and spectrum estimation techniques such as minimum-variance distortionless response beamforming (MVDR) beamforming [44], which generally achieve finer resolution than matched-filtering-based approaches underpinning techniques such as backprojection. The inclusion of the receive-beamforming enhancement and the phase constraint in (10) may condition the problem such that the diversity of scattering information available across sensor positions can be leveraged productively in the inverse problem. This may allow for achieving the resolution benefits of spectrum estimation in the range direction, even for a limited aperture.

The second important difference between the PE-LSM and backprojection images is that the regions of high image value in the former appear more continuous across the target surface. The more continuous appearance may be due to multiple factors. The PE-LSM solution is found by simultaneously leveraging the signal from all directions via the optimization in (8), and thus may account for shifts in the specular reflection point with sensor position. In

addition, there may be lateral smoothing effects from both the beamforming enhancement and the Tikhonov-like term in (8).

Overall, the visual fidelity of the PE-LSM reconstructions is arguably qualitatively better than the backprojection images. The finer range resolution may be the most significant factor contributing to the superiority of the PE-LSM images, as it provides for finer detail on the shape of the illuminated surfaces and thus potentially allows for more straightforward discernment of the target shape. The implication of the smoothing effects of the PE-LSM is more nuanced. In principle, a series of densely distributed focused point scatterer responses can provide reasonable geometric fidelity to a target surface. However, in the examples in Fig. 3, the visual fidelity of the point scatterer response distribution in the backprojection images is degraded by the coarseness of the achievable range resolution.

It is also clear that the PE-LSM imagery is significantly improved in fidelity compared to the standard LSM imagery in terms of the structural information in the imagery. As in our previous studies [38], [39], this demonstrates that using both the beamforming enhancement and the phase-delay constraint in the PE-LSM formulation allows for extracting richer target geometrical information compared to performing LSM without additional modifications. The results in this subsection arguably demonstrate that the
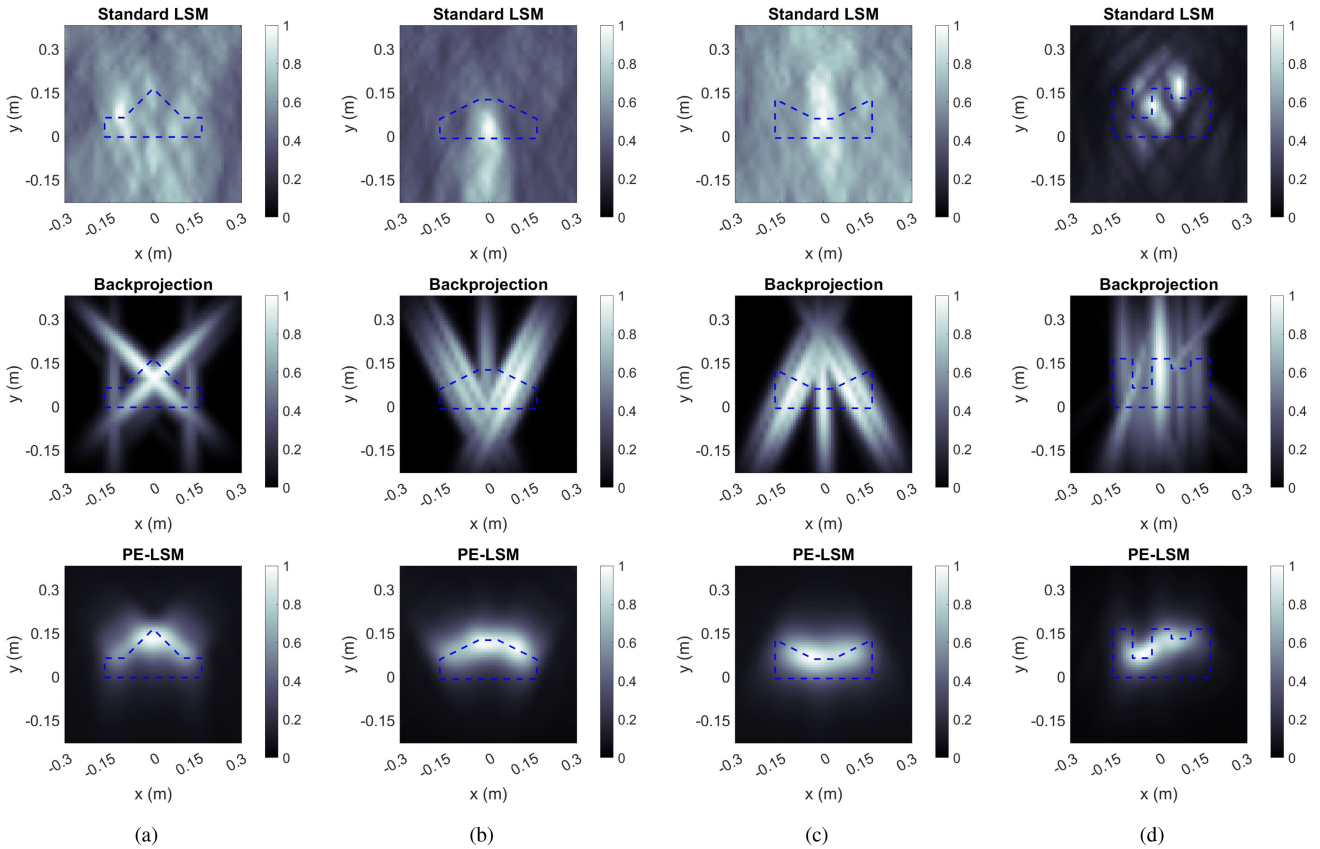
FIGURE 5. Images generated with only 0.25 GHz of bandwidth via the standard LSM, backprojection, and the PE-LSM for the (a) pedestal-and-triangle, (b) convex, (c) concave, and (d) double-cavity targets. The aperture is centered on the $+y$-axis.

PE-LSM outperforms both backprojection and the standard LSM for the limited synthetic aperture geometry.

B. EFFECTS OF VIRTUAL RECEIVER ANGULAR SPAN

Next, we consider how the distribution of virtual receivers affects the quality of the experimental images. In Fig. 4, we plot standard LSM, backprojection, and PE-LSM images for the double-cavity target using 0, 2, 4, and 8 virtual receivers. The spacing between virtual receivers is kept constant.

The backprojection images are nearly identical across all choices of virtual receivers. This demonstrates that the use of virtual receivers for backprojection provides little to no benefit compared to processing the monostatic data via a conventional synthetic aperture approach, as in Fig. 4(a). This also suggests that the conventional backprojection approach is not formulated to leverage the somewhat redundant signal information provided by closely spaced receivers moving in a synthetic aperture. We have observed identical behavior for the backprojection images across the targets in this study. We omit these images for conciseness.

The similarity in the backprojection images is also notable due to the plane-wave approximation in (14). The image in Fig. 4(a) uses no virtual receivers, and thus no plane-wave approximation. As the backprojection images in Fig. 4(b-d) are nearly identical, this suggest that the plane-wave

approximation in (14) does not degrade the backprojection images in this study that use virtual receivers.

In contrast to the backprojection images, both the standard LSM and PE-LSM images improve in lateral resolution as the span of virtual receivers increases. For the standard LSM, using no virtual receivers results in no discrimination between the target and the background. This is consistent with the general inability of the standard LSM to usefully leverage purely monostatic data. As more virtual receivers are added, the regions of high indicator function near the opening of the target cavities become more concentrated. However, the overall visual fidelity of the standard LSM images remains poor for all choices of virtual receiver.

For the PE-LSM, using no virtual receivers results in a region of high indicator function in the vicinity of the target. However, the fidelity of the reconstruction is poor due to limited lateral resolution. As the number of virtual receivers increases, the reconstruction improves in fidelity due to the improvement in lateral resolution. The PE-LSM reconstruction in Fig. 4(d), which uses nine virtual receivers, is very similar to the PE-LSM reconstruction in Fig. 3(d), which uses seven virtual receivers. This result suggests diminishing returns from adding additional virtual receivers and supports our choice of using seven virtual receivers in Section IV-A and all remaining subsections.

C. EFFECTS OF BANDWIDTH

In Fig. 5, we plot images for all four targets after decreasing the bandwidth of the signal to 0.25 GHz. We also decrease the spacing between selected frequency samples in order to again apply six frequencies to the imaging algorithms.

The standard LSM images are qualitatively very similar to the analogous images from Fig. 3, which used a much higher bandwidth of 1.25 GHz. This is consistent with expectations, as the LSM includes no mechanism for coherent processing across frequency and thus is somewhat limited in its ability to leverage multi-frequency information from limited apertures.

The apparent range resolution of both the backprojection and PE-LSM images appears degraded compared to the higher-bandwidth images from Fig. 3, which is also consistent with expectations. However, the image quality of the PE-LSM images has degraded more gracefully. The backprojection images evince long target responses that extend through nearly the entire imaging domain, which makes discernment of the true location and shape of the targets very difficult. In contrast, the PE-LSM indicator function remains concentrated in the vicinity of the target. While significant target detail has been lost compared to the PE-LSM images from Fig. 3, the target location as well as to some degree its lateral extent can be ascertained from the indicator function. This result suggests that the PE-LSM could potentially be particularly useful in synthetic aperture applications with low-bandwidth sensors.

D. IMAGES FROM NEARLY COMPLETE ROTATIONS

Lastly, we consider the performances of the algorithms for a target rotation of 350°. The 10° gap in the aperture is located on the $+x-$axis in the local coordinates of the processed images. The small gap is due to experimental challenges related to the rotational stage hardware. We once again use 1.25 GHz of bandwidth and seven virtual receivers. The results are plotted in Fig. 6.

The standard LSM images are again of relatively low fidelity. There is some improvement in concentration of the indicator function in the vicinity of the target compared to Fig. 3. This is most likely due to the availability of signal from multiple directions, which mitigates to some extent the lack of range information available from the limited aperture in Fig. 3. The indicator function is mostly concentrated near one or a few prominent scattering features, such as the bottom plate of each target or the opening of the voids of the double-cavity target. However, there is little additional target geometrical information discernible in the images. This is consistent with previous results from simulated data for full target rotations with only a few receivers [38].

The contrast of the standard LSM imagery is degraded compared to the limited-aperture cases in Fig. 3, especially for the double-cavity target. This may be because various scattering features are only visible to the sensor over portions of the synthetic aperture. Averaging effects from processing across the entire 350° may thus lower the apparent intensity of the brightest features in the image compared to less visible features and the background.

For the backprojection images, focused scatterer responses are now evident across nearly all target surfaces, with the exception of the surfaces on the far right sides of the targets due to the 10° gap in the target rotation. The fidelity of the distribution of focused responses across the illuminated surfaces is similar to the fidelity observed in Fig. 3.

The PE-LSM images in Fig. 6 also evince concentrated regions of increased indicator function along all illuminated edges of the target. As with the backprojection images, the rightmost surfaces of the target do not appear in the image due to the gap in the sensor aperture. The range resolution is again finer for the PE-LSM compared to backprojection. (For this nearly-full-aperture example, the range resolution corresponds to the direction pointing towards the center of the image from the feature of interest). A minor degradation in range resolution is evident compared to the limited-aperture PE-LSM images from Fig. 3. A possible explanation is that each target surface is not visible for all aperture locations due to shadowing and the impenetrability of the conducting targets. This may cause modest blurring due to averaging effects in the PE-LSM optimization. Interestingly, there is not a significant degradation of contrast from Fig. 3 comparable to the effect seen in the standard LSM imagery, especially for the double-cavity target, as discussed above. This suggests that the PE-LSM is less sensitive than the standard LSM to averaging effects caused by scattering features with limited visibility across angle. This may be due to the enhanced spatial focusing provided by the beamforming enhancement and the phase-delay constraint.

As in Section IV-A, the finer resolution of the PE-LSM images arguably allows for more straightforward visual discrimination of target shape compared to the backprojection images. For example, the backprojection images of the triangle-and-pedestal target in Fig. 6(a) and the convex target in Fig. 6(b) are somewhat similar in appearance and could require close inspection to distinguish. In contrast, the finer resolution of the PE-LSM images makes the differences in the shapes of the target features more obvious.

E. QUANTITATIVE FIDELITY EVALUATION

The results in the previous subsections demonstrated the superior fidelity of the PE-LSM images qualitatively. In this subsection, we support this analysis by evaluating fidelity with a quantitative metric.

Our chosen metric is the well-known Jaccard index. It gives a measure of how close the support of the reconstruction matches the true support of the target. It has thus been frequently used in inverse scattering studies where the goal is to reconstruct the target shape [39], [53], [54]. The Jaccard index is given by

$$J = \frac{I_{\text{thresh}}(\mathbf{r}) \cap T(\mathbf{r})}{I_{\text{thresh}}(\mathbf{r}) \cup T(\mathbf{r})}, \tag{22}$$
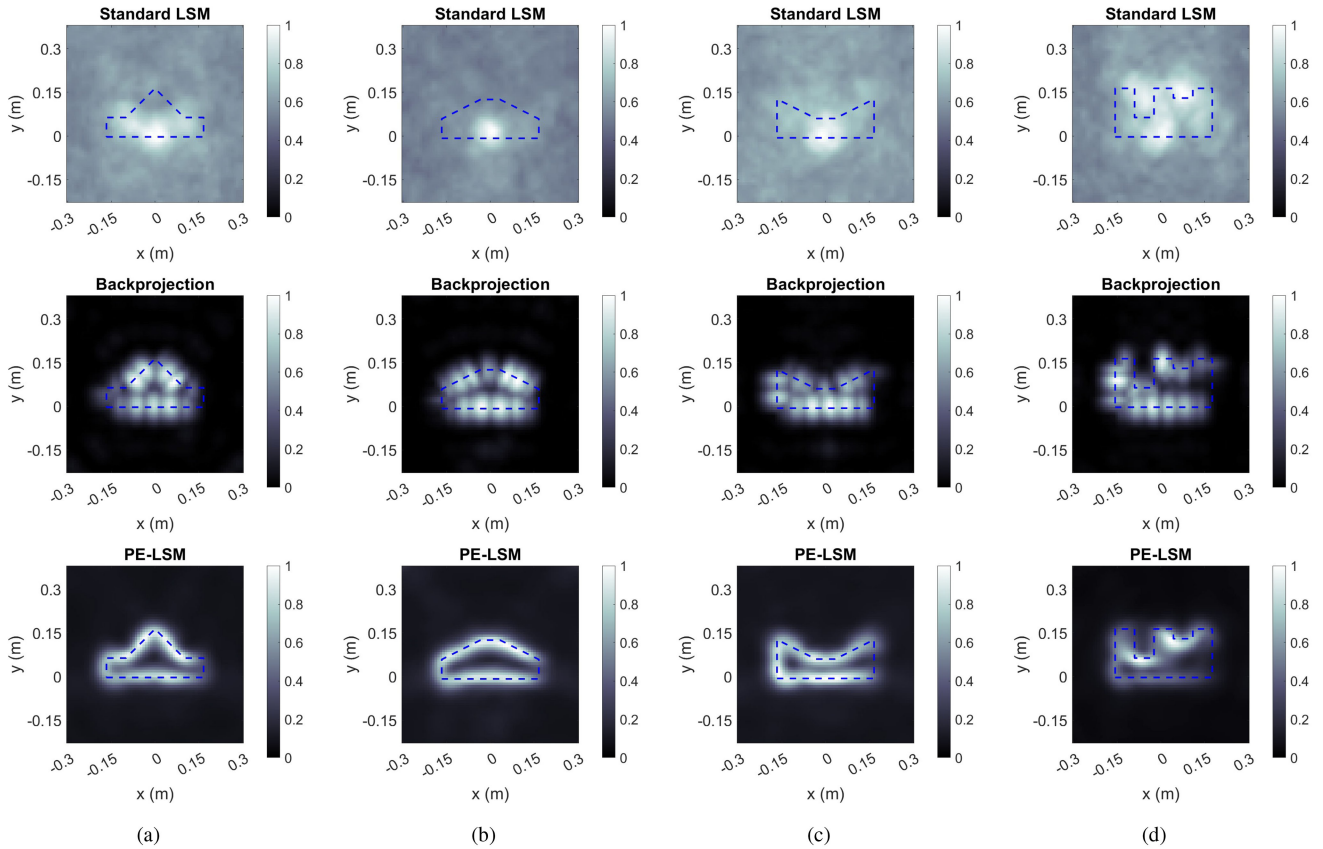
FIGURE 6. Images generated via the standard LSM, backprojection, and the PE-LSM from 350° apertures for the (a) pedestal-and-triangle, (b) convex, (c) concave, and (d) double-cavity targets. The 10° gap in the aperture is on the $+x$-axis.

where $T(\mathbf{r})$ is the reference used to represent the true target support and I_{thresh} is a thresholded version of the target image, where all pixels below a chosen threshold are set to zero and all pixels above the threshold are set to one. For each example, we calculate J over a series of thresholds ranging from 0.05 to 0.95. (As all images have been normalized to the most intense pixel, the maximum image intensity for all examples is 1). Higher Jaccard indices correspond to improved fidelity. A perfect match between $T(\mathbf{r})$ and $I_{\text{thresh}}(\mathbf{r})$ gives $J = 1$.

We construct $T(\mathbf{r})$ for use in (22) in order to account for the expected visibility of the target features for each aperture choice. As seen in Figs. 3-6, the target reconstructions emphasize the surfaces of the targets that are illuminated by the sensors. The target interiors and (in the limited-aperture cases) the sides of the targets on the opposite sides of the sensors are not reconstructed. This is expected, as these regions are not accessible to the electric fields due to the high conductivity of the target surfaces.

We therefore define $T(\mathbf{r})$ in the following manner. For each target and aperture choice, we define a binary grid of pixels of the same dimension as the target images. We identify surfaces that are on the same side of the target as the sensor aperture in each case. We define two layers of pixels that straddle each of these surfaces and fill them with
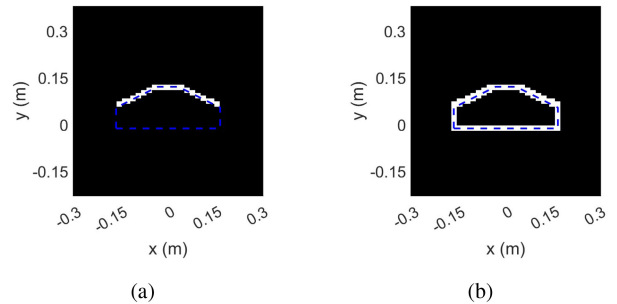
FIGURE 7. Target surfaces used for calculating the Jaccard index for the convex target for (a) 90° and (b) 350° apertures.

ones. The rest of the pixels are left as zeros. Examples of $T(\mathbf{r})$ for the convex target are given in Fig. 7(a) for the 90° target rotation and Fig. 7(b) for the 350° target rotation.

It is helpful to define $T(\mathbf{r})$ in this manner to capture imaging performance with context that is appropriate for the imaging scenario. For example, an imaging technique with low range resolution may place significant image energy into the interior of the target from target responses on its surface. Similarly, in a limited-aperture scenario, a low-resolution technique could place image energy onto shadowed surfaces. If $T(\mathbf{r})$ is defined to emphasize the inaccessible target interior
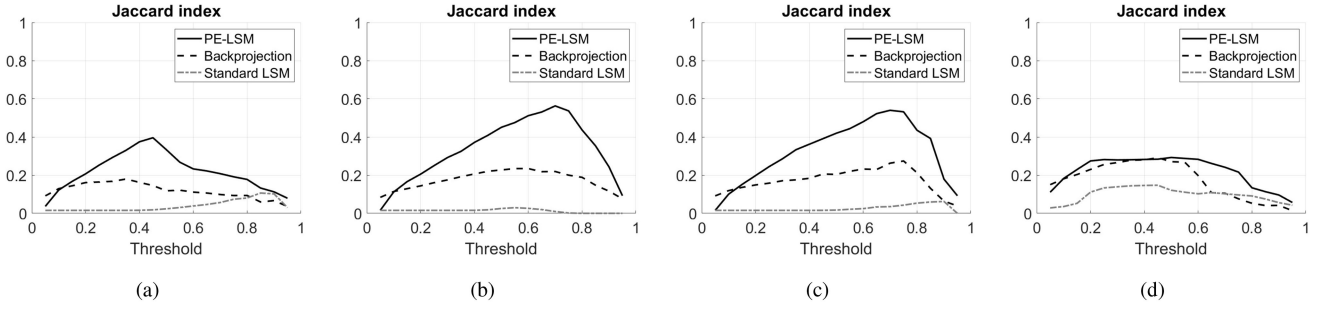
FIGURE 8. The Jaccard index for images from 90° rotations for the (a) pedestal-and-triangle, (b) convex, (c) concave, and (d) double-cavity targets.
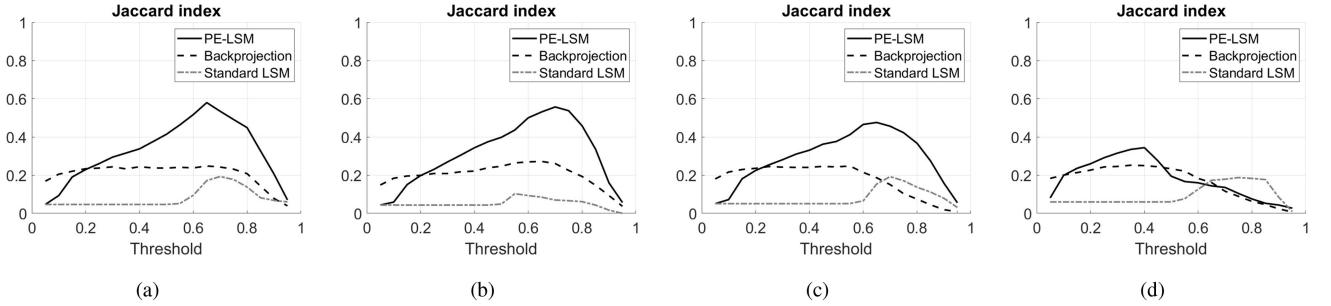

FIGURE 9. The Jaccard index for images from 350° rotations for the (a) pedestal-and-triangle, (b) convex, (c) concave, and (d) double-cavity targets.

or shadowed surfaces, then the technique's low resolution could result in a higher-than-deserved Jaccard index.

The Jaccard indices are plotted in Fig. 8 and Fig. 9 for 90° and 350° target rotations, respectively. In each case, 1.25 GHz of bandwidth and seven virtual receivers are used. The corresponding images are given in Fig. 3 and Fig. 6, respectively.

Across the targets, the PE-LSM achieves the highest J across a broad range of thresholds. For three of the four targets, including the triangle-and-pedestal, convex, and concave targets, the peak J for the PE-LSM results is significantly higher compared to both backprojection and the standard LSM, indicating significantly superior matches between the reconstructions and the target support references. This is most likely due to the higher range resolution of the PE-LSM which concentrates the indicator function along the target illuminated surfaces and thus within the layers of ones in $T(\mathbf{r})$.

Conversely, the standard LSM achieves the lowest J across broad ranges of thresholds. The peak J is significantly lower than the peak for PE-LSM and at least somewhat lower than the peak for backprojection for all examples. Across the targets, the Jaccard index plots are thus broadly consistent with our qualitative evaluation that the PE-LSM images achieve the highest visual fidelity, followed by the backprojection images and then the standard LSM images.

There are some nuances in the fidelity plots for the double-cavity target. For both aperture choices, the highest J is still achieved by the PE-LSM. However, for the limited-aperture case in Fig. 8(d), the peak J is nearly identical for PE-LSM and backprojection. The PE-LSM also achieves near-peak performance across a broader range of thresholds, which arguably indicates superior robustness. For the nearly-full-rotation case in Fig. 9(d), the PE-LSM peak J is higher than the backprojection peak J, but the difference is more modest compared to other targets.

The difference in the J curves between the double-cavity target and the other targets is most likely due to the differences in the PE-LSM indicator function across target surfaces. The indicator function in the cavity bottom surfaces is higher compared to the rest of the target. This is likely caused by the corner reflector responses from the bottom of the cavities, which may be stronger and more persistent across angle than the exterior surfaces. The corresponding backprojection images evince less variation in image intensity across the surfaces, perhaps due to the mitigation of anisotropic effects via the subaperture-based implementation.

F. COMPUTATIONAL EXPENSE

We generated the imagery for this study using a laptop with a 2.6 GHz Intel Xeon processor running MATLAB. For the limited-aperture scenarios in Section IV-A, the PE-LSM generates imagery in approximately one minute. For the nearly-full aperture scenarios in Section IV-D, the PE-LSM generates imagery in approximately 30 minutes.

The large increase in computation time for the nearly-full apertures is due to the increase in the size of the matrix system in (12). In particular, $\mathbf{I}$ and $\mathbf{D}$ scale with N_{tx} in both their numbers of rows as well as columns. The number of transmit positions N_{tx} is equivalent to the number of synthetic aperture samples in the monostatic scenarios of

interest. Thus, increasing the aperture size by around a factor of four results in computational expense that increases by significantly more than a factor of four due to the growth of the matrices in both dimensions.

To reduce the computational expense for the near-full aperture scenarios, we experimented with a strategy inspired by the subaperture approach described in Section II-E. We form a series of PE-LSM images for overlapping subapertures of size 87.5°. We choose this subaperture size to maintain a similar imaging performance as the limited apertures in Section IV-A while dividing evenly into 350°. With 50% overlap, this results in seven subapertures. We then form a composite image over the subapertures in the same fashion as (21), wherein the final indicator function value for each pixel is selected according to the maximum response across subapertures.

This subaperture strategy results in a reduction of PE-LSM computation time for the near-full-aperture scenarios from 30 minutes to approximately seven minutes. The lower computation time is due to the reduction of the matrices in (12) in both dimensions to a similar size as the matrices for the limited aperture scenarios in Section IV-A. Thus, processing across seven subapertures takes about seven times as long as processing across a single 90° aperture instead of 30 times as long. Further reduction in computation time could perhaps be achieved by leveraging parallel processing across the subapertures.

We have found that PE-LSM processing across subapertures in this manner results in very similar image fidelity as processing across the entire aperture. This is most likely because most target features are only visible for a single subaperture due to shadowing and anisotropic effects. Thus, the subaperture strategy is a promising approach for reducing PE-LSM computational expense for very wide apertures.

G. DISCUSSION

This study demonstrates experimentally that melding LSM principles with conventional radar principles allows for achieving multiple benefits. Compared to the LSM, the PE-LSM can better leverage range information in the multi-frequency signal and achieves significantly improved flexibility in sensor count and data acquisition geometry. Compared to backprojection, the PE-LSM can achieve finer range resolution, resulting in superior overall fidelity to the true target shape.

The resulting finer detail in the PE-LSM-reconstructed target shape could potentially provide more sensitivity for detecting changes in targets for applications such as non-destructive evaluation. Alternatively, it may allow for more detailed extraction of target geometry for applications such as target identification.

There are multiple potential avenues for future development of the PE-LSM. For instance, this study focused on the problem of reconstructing the shape of the target, in keeping with the primary goal of LSM-based imaging approaches. However, reconstructing some spatial mapping

of reflectivity or radar cross-section is potentially also of interest for evaluating target structure. Extracting radar cross-section is common for radar imaging techniques, and thus may also be possible in some form via the PE-LSM, given the similarity in the receive-beamforming enhancement and the phase-delay-constraint to radar processing principles. Indeed, the PE-LSM images in Figs. 3(d) and 6(d) provide some preliminary evidence of a connection between a strong scattering response and high indicator function values for some features. Robust extraction of such information via the PE-LSM and quantification of performance with appropriate metrics is deserving of its own dedicated study, as is leveraging the resulting information for target evaluation or identification.

Future work may also involve mitigating signal approximations used in the PE-LSM formulation. The enhancements composing the monostatic PE-LSM are Born approximated, including the receive beamforming enhancement in (9), the phase constraint in (10), and the integral equation underlying the monostatic-to-multistatic transformation in (14). (It is important to note that the Born approximation is also present in conventional backprojection). The formulation of the monostatic-to-multistatic transformation also includes a plane-wave approximation. Avoiding or mitigating these approximations could aid in extending the PE-LSM to various challenging scenarios. Such scenarios of interest could include imaging environments wherein the background propagation is complex due to a heterogeneous embedding medium.

Experimental validation for other scenarios is of interest for future studies. While this study focused on the challenge of imaging targets that are quite electrically large, it would also be interesting to validate performance for smaller targets. Our previous study on synthetic-aperture imaging with the PE-LSM included an experimental example with a conducting sphere that was only a wavelength or so in size [38]. Our previous limited-aperture simulated study of the PE-LSM also included targets of only a few wavelength in size [39]. Thus, imaging small targets with the PE-LSM appears feasible. However, given the limitations of existing datasets that we discuss in the introduction to this paper, robust experimental validation for smaller targets that are more geometrically complex will require collection of new data that is out of the scope of the present study. Other experimental scenarios of interest for future work include 3D scenarios, data acquisition strategies with a significant bistatic angular offset between the transmitter and receiver, and target scenes with disjoint scatterers.

Lastly, it is important to note that the data in this study were collected in an anechoic chamber, as in many previous inverse scattering studies [9], [19], [20], [21], [23], [35], [48], [54], and thus effects of interference, noise, and clutter were minimal. Future application-specific work may thus require evaluating robustness to these variables in application-relevant environments as well as developing mitigation strategies as necessary. However, our previous

numerical work [39] has suggested that the PE-LSM is more robust to noise compared to other LSM variants and outperforms or is competitive with backprojection for modest signal-to-noise ratios. Thus, the outlook for the PE-LSM is potentially promising in regards to challenges from perturbations in the data.

V. CONCLUSION

In this paper, we conducted an anechoic chamber study of the PE-LSM, which is a formulation of the well-known LSM that allows for limited-aperture and synthetic-aperture imaging of conducting targets. We advanced the study of the PE-LSM by evaluating performance against multiple targets with a variety of scattering features, whereas previous work used mostly simulated data and a single experimental example. Furthermore, we demonstrated good imaging performance using only a single transmitter and receiver. This is significant, as conventional LSM processing typically requires many multistatic sensor combinations to achieve fidelity and previous PE-LSM work has used at least a handful of multistatic receivers. This study thus represents a significant advance in the practicality of LSM-based processing.

Using the PE-LSM, we demonstrated significant improvements in fidelity of the reconstructed target shape compared to both the standard LSM and a radar backprojection formulation. Improved performance was evident both from qualitative evaluation of image fidelity as well as from a quantitative fidelity metric. The improved performance motivates continued study of the PE-LSM for extracting fine target detail for the purpose of non-destructive evaluation or target identification.

ACKNOWLEDGMENT

REFERENCES

[1] W. C. Chew and Y. M. Wang, "Reconstruction of two-dimensional permittivity distribution using the distorted born iterative method," *IEEE Trans. Med. Imag.*, vol. 9, no. 2, pp. 218–225, Jun. 1990.

[2] Y. M. Wang and W. C. Chew, "An iterative solution of the two-dimensional electromagnetic inverse scattering problem," *Int. J. Imag. Syst. Technol.*, vol. 1, no. 1, pp. 100–108, 1989.

[3] T. J. Cui, W. C. Chew, A. A. Aydiner, and S. Chen, "Inverse scattering of two-dimensional dielectric objects buried in a lossy earth using the distorted born iterative method," *IEEE Trans. Geosci. Remote Sens.*, vol. 39, no. 2, pp. 339–346, Feb. 2001.

[4] P. M. Van den Berg and A. Abubakar, "A contrast source inversion method," *Inverse Problems*, vol. 13, no. 6, pp. 1607–1620, 1997.

[5] C. Gilmore, P. Mojabi, and J. LoVetri, "Comparison of an enhanced distorted born iterative method and the multiplicative-regularized contrast source inversion method," *IEEE Trans. Antennas Propag.*, vol. 57, no. 8, pp. 2341–2351, Aug. 2009.

[6] L. Poli, G. Oliveri, and A. Massa, "Imaging sparse metallic cylinders through a local shape function Bayesian compressive sensing approach," *J. Opt. Soc. Am. A, Opt. Image Sci. Vis.*, vol. 30, no. 6, pp. 1261–1272, 2013.

[7] T. Takenaka, Z. Q. Meng, T. Tanaka, and W. C. Chew, "Local shape function combined with genetic algorithm applied to inverse scattering for strips," *Microw. Opt. Technol. Lett.*, vol. 16, no. 6, pp. 337–341, Dec. 1997.

[8] G. P. Otto and W. C. Chew, "Microwave inverse scattering–local shape function imaging for improved resolution of strong scatterers," *IEEE Trans. Microw. Theory Techn.*, vol. 42, no. 1, pp. 137–141, Jan. 1994.

[9] X. Ye, "Electromagnetic imaging of wave impenetrable objects," in *Proc. 11th Eur. Conf. Antennas Propag. (EUCAP)*, 2017, pp. 1424–1428.

[10] X. Ye, X. D. Chen, Y. Zhong, and K. Argawal, "Subspace-based optimization method for reconstructing perfectly electric conductors," *Prog. Electrom. Res.*, vol. 100, pp. 119–218, Dec. 2010.

[11] X. Ye, Y. Zhong, and X. Chen, "Reconstructing perfectly electric conductors by the subspace-based optimization method with continuous variables," *Inverse Problems*, vol. 27, no. 5, May 2011, Art. no. 055011.

[12] J. Shen, Y. Zhong, X. Chen, and L. Ran, "Inverse scattering problems of reconstructing perfectly electric conductors with TE illumination," *IEEE Trans. Antennas Propag.*, vol. 61, no. 9, pp. 4713–4721, Sep. 2013.

[13] M. R. Hajihashemi and M. El-Shenawee, "Shape reconstruction using the level set method for microwave applications," *IEEE Antennas Wireless Propag. Lett.*, vol. 7, pp. 92–96, 2008.

[14] M. R. Hajihashemi and M. El-Shenawee, "TE versus TM for the shape reconstruction of 2-D PEC targets using the level-set algorithm," *IEEE Trans. Geosci. Remote Sens.*, vol. 48, no. 3, pp. 1159–1168, Mar. 2010.

[15] M. R. Hajihashemi and M. El-Shenawee, "Inverse scattering of three-dimensional PEC objects using the level-set method," *Prog. Electromagn. Res.*, vol. 116, pp. 23–47, Apr. 2011.

[16] M. N. Stevanovic, L. Crocco, A. R. Djordjevic, and A. Nehorai, "Higher order sparse microwave imaging of PEC scatterers," *IEEE Trans. Antennas Propag.*, vol. 64, no. 3, pp. 988–997, Mar. 2016.

[17] N. Vojnovic, M. N. Stevanovic, L. Crocco, and A. R. Djordjevic, "High-order sparse shape imaging of PEC and dielectric targets using TE polarized fields," *IEEE Trans. Antennas Propag.*, vol. 66, no. 4, pp. 2035–2043, Apr. 2018.

[18] M. M. Nikolic, A. Nehorai, and A. R. Djordjevic, "Electromagnetic imaging of hidden 2-D PEC targets using sparse-signal modeling," *IEEE Trans. Geosci. Remote Sens.*, vol. 51, no. 5, pp. 2707–2721, May 2013.

[19] M. Bevacqua and T. Isernia, "Shape reconstruction via equivalence principles, constrained inverse source problems and sparsity promotion," *Prog. Electromagn. Res.*, vol. 158, pp. 37–48, Feb. 2017.

[20] M. T. Bevacqua and R. Palmeri, "Qualitative methods for the inverse obstacle problem: A comparison on experimental data," *J. Imaging*, vol. 5, no. 4, p. 47, Apr. 2019.

[21] S. Sun, B. J. Kooij, A. G. Yarovoy, and T. Jin, "A linear method for shape reconstruction based on the generalized multiple measurement vectors model," *IEEE Trans. Antennas Propag.*, vol. 66, no. 4, pp. 2016–2025, Apr. 2018.

[22] F.-F. Wang and Q. H. Liu, "A bernoulli–gaussian binary inversion method for high-frequency electromagnetic imaging of metallic reflectors," *IEEE Trans. Antennas Propag.*, vol. 68, no. 4, pp. 3184–3193, Apr. 2020.

[23] F. Soldovieri, A. Brancaccio, G. Leone, and R. Pierri, "Shape reconstruction of perfectly conducting objects by multiview experimental data," *IEEE Trans. Geosci. Remote Sens.*, vol. 43, no. 1, pp. 65–71, Jan. 2005.

[24] R. Solimene, A. Buonanno, F. Soldovieri, and R. Pierri, "Physical optics imaging of 3-D PEC objects: Vector and multipolarized approaches," *IEEE Trans. Geosci. Remote Sens.*, vol. 48, no. 4, pp. 1799–1808, Apr. 2010.

[25] D. Colton, H. Haddar, and M. Piana, "The linear sampling method in inverse electromagnetic scattering theory," *Inverse Problems*, vol. 19, no. 6, p. S105, 2003.

[26] F. Cakoni and D. Colton, "The linear sampling method for cracks," *Inverse Problems*, vol. 19, no. 2, p. 279–295, 2003.

[27] F. Cakoni, D. Colton, and H. Haddar, "The linear sampling method for anisotropic media," *J. Comp. App. Math.*, vol. 146, pp. 285–299, Sep. 2002.

[28] D. Colton and P. B. Monk, "Target identification of coated objects," *IEEE Trans. Antennas Propag.*, vol. 54, no. 4, pp. 1232–1242, Apr. 2006.

[29] M. G. Aram, M. Haghparast, M. S. Abrishamian, and A. Mirtaheri, "Comparison of imaging quality between linear sampling method and time reversal in microwave imaging problems," *Inverse Problems Sci. Eng.*, vol. 24, no. 8, pp. 1347–1363, 2016.

[30] Y. Guo, P. Monk, and D. Colton, "The linear sampling method for sparse small aperture data," *Appl. Anal.*, vol. 95, no. 8, pp. 1599–1615, 2016.

[31] B. B. Guzina, F. Cakoni, and C. Bellis, "On the multi-frequency obstacle reconstruction via the linear sampling method," *Inverse Problems*, vol. 29, Nov. 2010, Art. no. 125005.

[32] M. Cheney, "The linear sampling method and the MUSIC algorithm," *Inverse Problems*, vol. 17, no. 4, pp. 591–595, 2000.

[33] F. Collino, M. Fares, and H. Haddar, "On the validation of the linear sampling method in electromagnetic inverse scattering problems," in *Proc. 6th Int. Conf. Math. Numer. Aspects Wave Propag.*, 2003, pp. 649–654.

[34] N. Shelton and K. F. Warnick, "Behavior of the regularized sampling inverse scattering method at internal resonance frequencies," *Prog. Electrom. Res.*, vol. 38, pp. 29–45, 2002.

[35] I. Catapano, L. Crocco, and T. Isernia, "On simple methods for shape reconstruction of unknown scatterers," *IEEE Trans. Antennas Propag.*, vol. 55, no. 5, pp. 1431–1436, May 2007.

[36] M. Ambrosanio, M. T. Bevacqua, T. Isernia, and V. Pascazio, "Performance analysis of tomographic methods against experimental contactless multistatic ground penetrating radar," *IEEE J. Sel. Topics Appl. Earth Obs. Remote Sens.*, vol. 14, pp. 1171–1183, 2021.

[37] F. Cakoni, M. Fares, and H. Haddar, "Analysis of two linear sampling methods applied to electromagnetic imaging of buried objects," *Inverse Problems*, vol. 22, no. 3, pp. 845–867, 2006.

[38] M. J. Burfeindt and H. F. Alqadah, "Phase-encoded linear sampling method imaging of conducting surfaces from full and limited synthetic apertures," *IEEE Open J. Antennas Propag.*, vol. 3, pp. 1191–1205, 2022.

[39] M. Burfeindt and H. Alqadah, "Linear sampling method imaging of three-dimensional conducting targets from limited apertures via phase-delay-constrained formulations," *Prog. Electrom. Res.*, vol. 178, pp. 63–81, Oct. 2023.

[40] M. J. Burfeindt, S. Ziegler, and H. F. Alqadah, "Fidelity evaluation of the phase-encoded linear sampling method and backprojection imaging," in *Proc. IEEE APS/URSI Conf.*, 2023, pp. 261–262.

[41] M. Ambrosanio, M. T. Bevacqua, T. Isernia, and V. Pascazio, "Experimental multistatic imaging via the linear sampling method," in *Proc. IEEE Int. Geosci. Remote Sens. Symp.*, 2019, pp. 3586–3589.

[42] M. Ambrosanio, M. T. Bevacqua, V. Pascazio, and T. Isernia, "Qualitative imaging of experimental multistatic ground penetrating radar data," in *Proc. Eur. Conf. Ant. Propag.*, 2020, pp. 1–4.

[43] H. F. Alqadah and M. Burfeindt, "A far-field transformation procedure for monostatic linear sampling method imaging," in *Proc. Int. Conf. Electromag. Adv. Appl. (ICAA)*, 2019, pp. 1387–1392.

[44] H. F. Alqadah and M. J. Burfeindt, "An adaptive monostatic inverse scattering approach using virtual multistatic geometries," in *Proc. IEEE Radar Conf.*, 2023, pp. 1–6.

[45] C. Gilmore, A. Zakaria, P. Mojabi, M. Ostadrahimi, S. Pistorius, and J. Lo Vetri, "The university of manitoba microwave imaging repository: A two-dimensional microwave scattering database for testing inversion and calibration algorithms," *IEEE Antennas Propag. Mag.*, vol. 53, no. 5, pp. 126–133, 2011.

[46] K. Belkebir and M. Saillard, "Special section: Testing inversion algorithms against experimental data," *Inverse Problems*, vol. 17, no. 6, pp. 1565–1571, 2001.

[47] I. Catapano, L. Crocco, and T. Isernia, "Improved sampling methods for shape reconstruction of 3-D buried targets," *IEEE Trans. Geosci. Remote Sens.*, vol. 46, no. 10, pp. 3265–3273, Oct. 2008.

[48] P. Monk, M. Pena, and V. Selgas, "Multifrequency linear sampling method on experimental datasets," *IEEE Trans. Antennas Propag.*, vol. 71, no. 11, pp. 8788–8798, Nov. 2023.

[49] M. Soumekh, *Synthetic Aperture Radar Signal Processing with MATLAB Algorithms*. New York, NY, USA: Wiley, 1999.

[50] J. Ash, E. Ertin, L. C. Potter, and E. Zelnio, "Wide-angle synthetic aperture radar imaging," *IEEE Signal Process. Mag.*, vol. 34, no. 4, pp. 16–26, Jul. 2014.

[51] B. D. Rigling, "Episodic processing for characterization of wide-angle SAR scattering behavior," in *Proc. SPIE Defense Commer. Sens. Conf., Algorithms Synth. Aperture Radar Imagery*, 2021, pp. 89–100.

[52] E. Ertin, C. Austin, S. Sharma, R. Moses, and L. Potter "GOTCHA experience report: Three-dimensional SAR imaging with complete circular apertures," in *Proc. SPIE Defense Secur. Symp., Algorithms Synth. Aperture Radar Imagery*, 2007, pp. 9–20.

[53] K. H. Leem, J. Liu, and G. Pelekanos, "Two direct factorization methods for inverse scattering problems," *Inverse Problems*, vol. 34, no. 12, 2018, Art. no. 125004.

[54] M. N. Akıncı, M. Çayören, and I. Akduman, "Near-field orthogonality sampling method for microwave imaging: Theory and experimental verification," *IEEE Trans. Microw. Theory Techn.*, vol. 64, no. 8, pp. 2489–2501, Aug. 2016.